Texas A&M University
Mechanical Engineering Department
Turbomachinery Laboratory
Tribology Group

Measurements of Drag Torque, Lift Off Speed and Identification of Structural Stiffness and Damping in a Metal Mesh Foil Bearing

Research Progress Report to the TAMU Turbomachinery Research Consortium

TRC– B&C-3-09

by

Luis San Andrés
Mast-Childs Professor
Principal Investigator

Thomas Abraham Chirathadam
Research Assistant

May 2009
Continuation (Year II)
Period of Performance: September 1, 2008 – May 31, 2009

Metal Mesh-Top Foil Bearings for Oil-Free
Turbomachinery: Test Rig for Prototype Demonstrations
TRC Funded Project, TEES # 32513/1519 V2

EXECUTIVE SUMMARY

Measurements of Drag Torque, Lift Off Speed and Identification of Structural Stiffness and Damping in a Metal Mesh Foil Bearing

Metal mesh foil bearings (MMFBs) are a promising low cost gas bearing technology for high speed oil-free microturbomachinery. Elimination of complex oil lubrication and sealing system by installing MMFBs in rotorcraft gas turbine engines offer distinctive advantages such as reduced system overall weight, enhanced reliability at high rotational speeds and extreme temperatures, and extended maintenance intervals compared to conventional engines. MMFBs for oil-free rotorcraft engines must demonstrate adequate load capacity, reliable rotordynamic performance, and low frictional losses in a high temperature environment. The report presents the measurements of MMFB break-away torque, rotor lift off and touchdown speeds, temperature at increasing static load conditions, and identified stiffness and equivalent viscous damping coefficients. The experiments, conducted in a test rig driven by an automotive turbocharger turbine, demonstrate the airborne operation (hydrodynamic gas film) of the floating test MMFB with little frictional loses at increasing loads. The measured drag torque peaks when the rotor starts and stops, and drops significantly once the bearing is airborne. The estimated rotor speed for lift-off increases linearly with increasing applied loads. During continuous operation, the MMFB temperature measured at one end of the back surface of the top foil increases both with rotor speed and static load. Nonetheless, the temperature rise is only nominal ensuring reliable bearing performance. Application of a sacrificial layer of solid lubricant on the top foil surface aids to reduce the rotor break-away torque. The measurements give confidence on this simple bearing technology for ready application into oil-free turbomachinery.

Impact loads delivered (with a soft tip) to the test bearing, while resting on the (stationary) drive shaft, evidence a system with large damping and a structural stiffness that increases slightly with frequency (max. 125 Hz). The system damping ratio decreases from ~ 0.94 to 0.47 as the frequency increases. In general, the viscous damping in a metal mesh structure is of structural type and inversely proportional to the frequency and amplitude of motion.

CIATEQ A.C., a TRC member, donated two aluminum foam bearings; their viability for use in turbomachinery is not recommended due to delicate integrity of the stiff metal foam.

Dear reader: The PI read, revised, edited (language and technical content) and rewrote every sentence of this report prior to its release to TRC members. The PI time and efforts are not rewarded by TRC funding structure.

TABLE OF CONTENTS

LIST OF TABLES

LIST OF FIGURES

NOMENCLATURE

$\{a_i\}_{i=X,Y}$	Acceleration of bearing cartridge along X and Y directions [m/s^2]
C_{crit}	Critical damping [Ns/m]
D	Diameter of rotating shaft [m]
D_{Bi}	Bearing cartridge inner diameter [m]
D_{Bo}	Bearing cartridge outer diameter [m]
D_{MMi}	Metal mesh ring inner diameter [m]
D_{MMo}	Metal mesh ring outer diameter [m]
D_W	Metal wire diameter [m]
E	Young's Modulus [N/m^2]
f	Friction coefficient [-]
$\{f_i\}_{i=X,Y}$	External excitation force [N]
f_n	Test system natural frequency [Hz]
F_Y	Impact force in frequency domain [N]
K_{est}	Estimated stiffness [N/m]
$\{K_{ij}, C_{ij},\}_{i,j=X,Y}$	Bearing stiffness [N/m] and equivalent viscous damping coefficients[Ns/m]
L	Bearing axial length [m]
M, M_{est}	Measured and estimated MMFB mass [kg]
M_m	Metal mesh ring mass [kg]
P	Power loss [W]
R	Radius of the rotating shaft [m]
R_i	Metal mesh ring inner radius [m]
R_o	Metal mesh ring outer radius [m]
T_{tf}	Top foil thickness [m]
U_d, U_v, U_f	Uncertainty in displacement[mm], voltage[V] and force[lb] respectively
W	Total static load on the bearing [N]
W_S	Applied static load [N]
W_D	Dead weight of the bearing assembly [N]
ρ_{MM}	Wire density = metal mesh mass/ (metal mesh volume× density of metal)
υ	Poisson's Ratio
ω	Excitation frequency [Hz]
$\{\delta i\}_{i=X,Y}$	Relative displacement of bearing with respect to the rotating shaft [m]

I. INTRODUCTION

Oil-free microturbomachinery (< 250 kW) implements gas bearings as they offer distinctive advantages like low friction, absence of complex lubrication systems, reliability and long operating life with little need of maintenance [1]. In a gas foil bearing, the hydrodynamic pressure generated within a small gap between the rotating shaft and a smooth foil supports a load. Gas foil bearings are presently used in air cycle machines, cryogenic turbocompressors and turboexpanders, and micro gas turbines. Gas bearings have potential application in high speed rotor bearing systems with moderate loads (static and dynamic) such as in fuel cell electric power systems, automotive turbochargers, etc [2].

Metal mesh foil bearings (MMFB) comprise of a top foil supported on a ring shaped metal mesh (MM) providing structural stiffness and mechanical energy dissipation with material hysteresis or dry-friction [3]. The current research on MMFBs modifies a patented gas bearing with an elastic porous material underneath a smooth top foil [4]. Figure 1 taken from Ref. [4] shows that the bearing consists of a bearing cartridge (a), an external circular (cartridge shim) foil (b), a resilient porous material support (c), and a top circular smooth foil (d). The trailing edges of the top circular foil, porous material and external circular (cartridge shim) foil are pinned at (g) and the top foil leading edges are free. The external circular (cartridge shim) foil facilitates seamless installation of the porous material inside the bearing cartridge. As the rotor (e) speed increases, a hydrodynamic film pressure (f) builds up and separates the rotor from the top foil.

Metal mesh foil bearings aim to satisfy the requirements for light, inexpensive, high power density (power per unit mass) gas turbines and automobile turbochargers, for example. The elimination of lubricating oil in MMFBs enhances the bearing reliability at high rotational speeds and extreme temperatures. MMFBs for oil-free turbomachinery require of adequate load capacity, reliable rotordynamic performance, and low frictional losses in a high temperature environment.

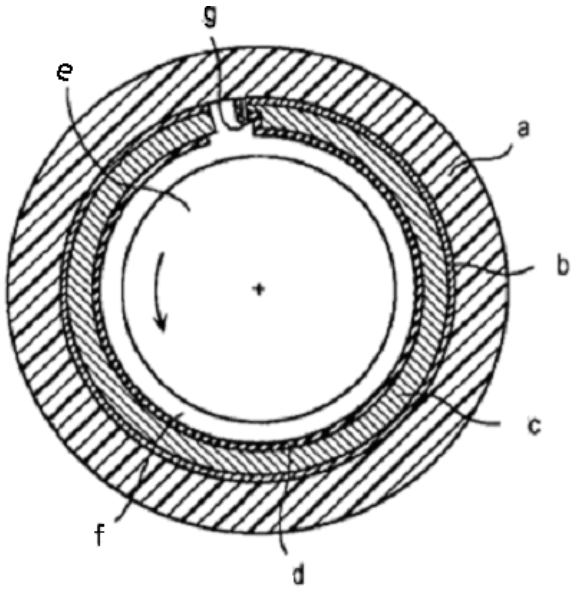

Fig. 1 Air foil bearing with a porous material support [4], (a) bearing cartridge, (b) external circular (cartridge shim) foil, (c) porous material support, (d) top circular foil, (e) rotating shaft, (f) hydrodynamic air film and (g) pinned edge. Patent No. WO 2006/043736 A1

The current metal mesh foil bearing design follows the concept illustrated in Figure 1, but installs a commercially available metal mesh ring between the top foil and the bearing cartridge, as depicted in Figure 2, to provide structural stiffness and damping. Note that prior experiments conducted at the Turbomachinery laboratory (TL) have demonstrated that metal mesh materials render equivalent viscous damping large enough to replace oil-lubricated squeeze film dampers, for example [5].

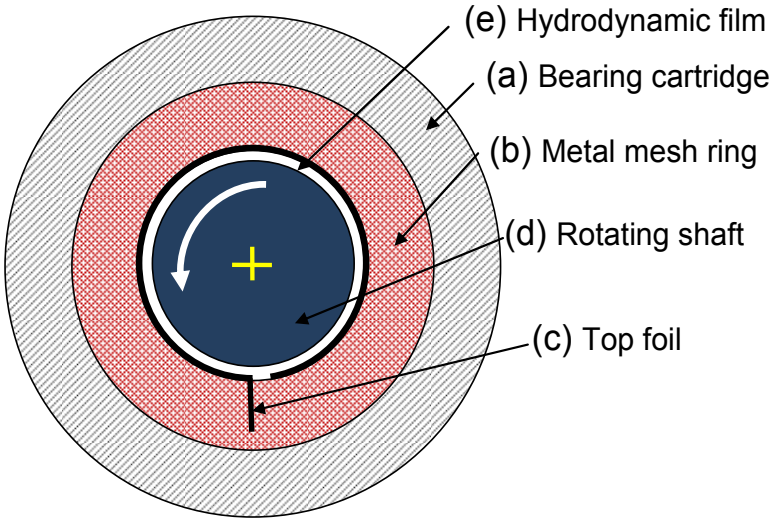

Fig. 2 Schematic view of a metal mesh foil bearing

San Andfes et al. [6] present the estimated structural stiffness and damping of a MMFB, obtained from static and dynamic load tests. Static load versus bearing deflection measurements show a nonlinear load-deflection relationship with a large mechanical hysteresis, indicating large mechanical energy dissipation. As depicted on Figure 3, the estimation of bearing stiffness, using the real part of the transfer function and measured mass of the bearing, shows a decrease (~ 40 %) in magnitude with an increase in frequency from 25 to 400 Hz, and decreases (~50%) with an increase in amplitude of motion from 12.7 µm to 38.1 µm. At the lowest test frequency of 25 Hz, the equivalent viscous damping coefficient attains the highest magnitude (~5.5 kNs/m and 3.6 kNs/m for 12.7 µm and 38.1 µm motion amplitudes respectively). Figure 4 shows that the equivalent viscous damping coefficient decays exponentially for increasing test frequencies. For the entire range of test frequencies, the MMFB equivalent viscous damping reduces with increase in motion amplitudes. The hysteretic damping property of the metal mesh ring is best represented with a loss factor (γ) defined as the ratio of the imaginary part of the mechanical impedance to the bearing stiffness. Figure 5 shows that the identified loss factor is as high as 0.50, a large magnitude for the simple bearing configuration, and exhibits little dependency on excitation frequency. However, later experiments show a reduction in MMFB stiffness and damping coefficients after multiple dismantling and reassembly processes and continuous operation.

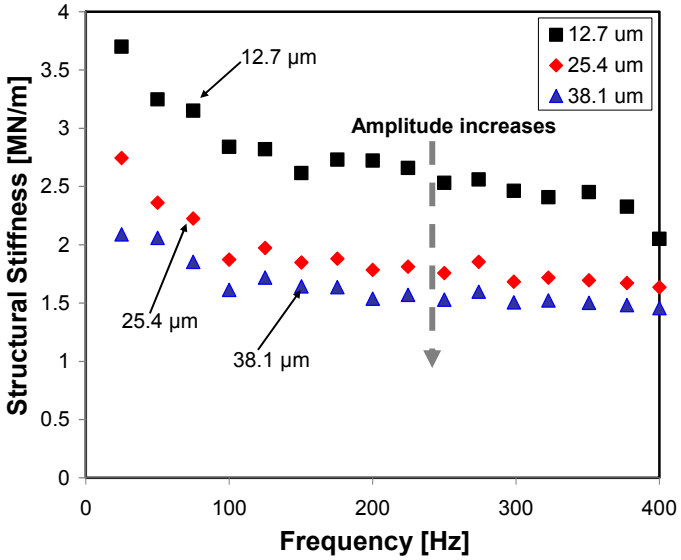

Fig. 3 MMFB structural stiffness *(K)* versus frequency derived from three motion amplitudes (12.7 µm, 25.4 µm, 38.1 µm). Ref. [6]

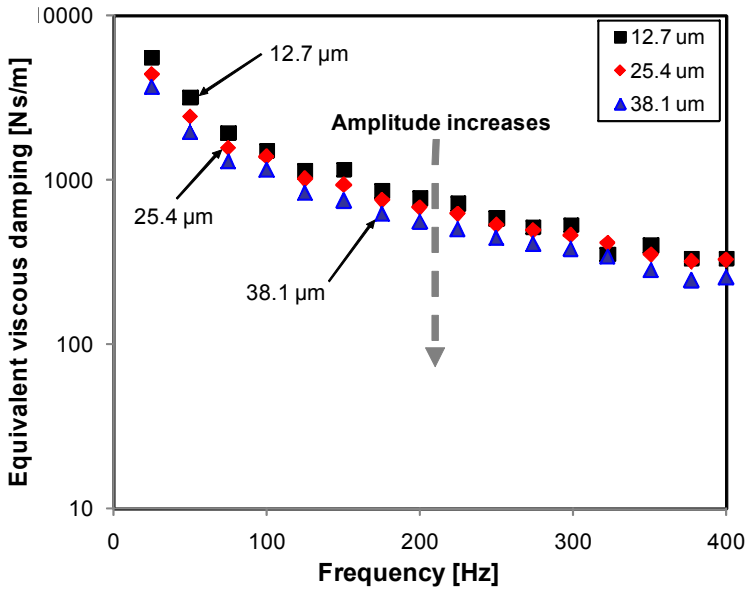

Fig. 4 Equivalent viscous damping versus frequency of excitation derived from three motion amplitudes (12.7 µm, 25.4 µm, 38.1 µm). Ref. [6]

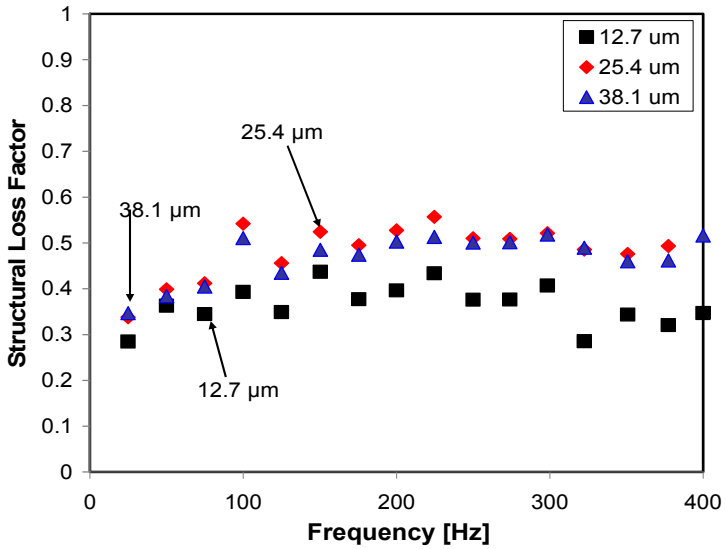

Fig. 5 Structural loss factor (γ) versus frequency of excitation derived from three motion amplitudes (12.7 µm, 25.4 µm, 38.1 µm). Ref. [6]

The present work advances prior research [6] by measuring the dynamic forced response of MMFBs. The bearing stiffness and damping coefficients are estimated from the rotor response to impact loads for various rotor speeds and applied static loads. A squirrel cage softly supports the test bearing in a turbocharger driven test rig and eddy current sensors measure the motion of the test journal relative to the bearing along two orthogonal directions. The measurement of bearing drag torque, temperature rise and load capacity for various static loads and operating speed

conditions will provide the information required for the application of metal mesh foil bearings in oil-free rotating machinery.

II. LITERATURE REVIEW

This literature review discusses prior work on the experimental identification and predictions of load capacity of foil bearings and the various techniques implemented to improve foil bearing load capacity.

In 1897, Kingsbury introduced the first self-acting air journal bearing [7], in which a minute hydrodynamic air film formed between the bearing and its rotating shaft supports a load. In 1953, Block and Van Rossum [8] presented the compliant surface foil bearing that has a larger hydrodynamic film thickness compared to rigid gas bearings, increasing its operational reliability and removing the stringent requirement for tight manufacturing clearances. Agrawal [1] presents an overview of foil bearing technology summarizing its chronological development during the last quarter of the 20th century. The author lists several applications of foil gas bearings like air cycle machines, vapor cycle machines, cryogenic turbo pumps, high speed fans for space stations, turbo expanders, high temperature auxiliary power unit for aircrafts, and a missile engine incorporating hot end foil bearings. The successful application of a foil bearing technology in high speed oil-free machinery requires of low drag torque, during start up and shut down, and sufficient load carrying capacity in the typical operating range of 20 – 70 krpm.

DellaCorte and Valco [9] introduce an empirically based 'rule of thumb' relating the bearing load capacity to the bearing size and rotor speed. The earliest bump type foil bearings (Generation I) have a low load because of their single bump foil strip with near uniform stiffness in the radial and circumferential directions. Generation II bearings with bump strips designed for a circumferentially varying stiffness double the load capacity. Further optimization of the bump strip layers with varying radial stiffness (Generation III) shows a more than two fold increase in load capacity. Advanced foil bearings, with compliance tailored elastic support structures, exhibit load capacities up to five times that of the initial simple designs.

DellaCorte [10] presents a high temperature test rig to measure the drag torque in foil bearings during multiple startup and shutdown cycles and reaching rotational speeds to 70 krpm. The test bearing has inner diameter and length of 35 mm and 25 mm, respectively. The test results show that the bearing drag torque is large just before rotor lift off, and immediately after

rotor touchdown, due to rubbing contact between the journal and the top foil surface. Once the bearing is airborne, the drag torque reduces to a minimum, and then increases gradually with rotor speed. In further tests in Ref. [11], the foil bearing torque increases with static load and decreases with operating temperature. The frictional force and contact stress between the top foil and the shaft surface contributes to the large drag torque at start up. The load capacity is estimated by coasting down the rotor from a high speed, while a static load is applied on the foil bearing, until the drag torque suddenly rises indicating the onset of rubbing. In a gas bearing, the load capacity approaches a limit, not increasing further with surface speed. The experimental load capacity in the test bearing is linear with speed to 30 krpm. It is speculated that a foil bearing reaches its ultimate load capacity when the minimum film thickness approaches the combined surface roughness of the top foil and the rotating shaft [11]. In the tests, the foil bearing load capacity decreases with increasing operating temperature, possibly due to the decrease in the support structure stiffness. Note that the ultimate load capacity of a foil bearing cannot exceed that of its resilient support structure, i.e. the bump strip layers.

Radil et al. [12] reports that the load capacity of a Generation III foil bearing, with inner diameter of 35 mm and length 25 mm and constructed from several nickel based super alloy foils, is the highest for a near optimum clearance. Note that clearance in a foil bearing is a vague concept since in actuality, upon assembly, no physical gap exists between a top foil and a stationary shaft. Continuous operation of a foil bearing that has a suboptimal clearance results in thermal runaway failure and seizure. However, a foil bearing can be operated safely with a radial clearance larger than the optimal value, but at a reduced load capacity. Ref. [13] shows that tailoring the support structure, to reduce the side leakage and to provide a uniform film thickness, results in a higher load capacity.

Peng and Khonsari [14] determine the ultimate load capacity of ideal foil bearings, showing its dependency on the stiffness (compliance) of the support structure beneath the top foil. Kim and San Andŕes [15] further advance the analysis to determine the effect of assembly preload on the ultimate load capacity for gas foil bearing operation at ultra high operating speeds. Note that foil bearings are typically assembled with a slight preload, i.e., the inner diameter of the top foil bring smaller than the journal diameter.

The current research does not focus on the tribological characteristics [16, 17] of solid lubricant coatings on the top foil and the rotating shaft.

III. DESCRIPTION OF TEST BEARING AND EXPERIMENTAL FACILITY

TEST METAL MESH FOIL BEARING

Figure 6 shows the photograph of a prototype bearing and Table 1 describes the three main components comprising a MMFB. The MMFBs employ commercially available ring shaped metal mesh as the elastic support under a thin top foil. The prototype bearing uses a metal mesh ring made of copper wires, owing to the large structural damping offered by copper meshes [3]. The top foil, a smooth arcuate surface 127μm thick, is in contact with the journal when not in operation. Note that, at high rotor speed operation, a thin hydrodynamic air film separates the top foil and the rotating journal. Hence, any wear of the journal or the bearing is absent while the rotor is airborne. In MMFBs, the metal mesh supporting the top foil also provides material damping and dry-friction energy dissipation effects [3].

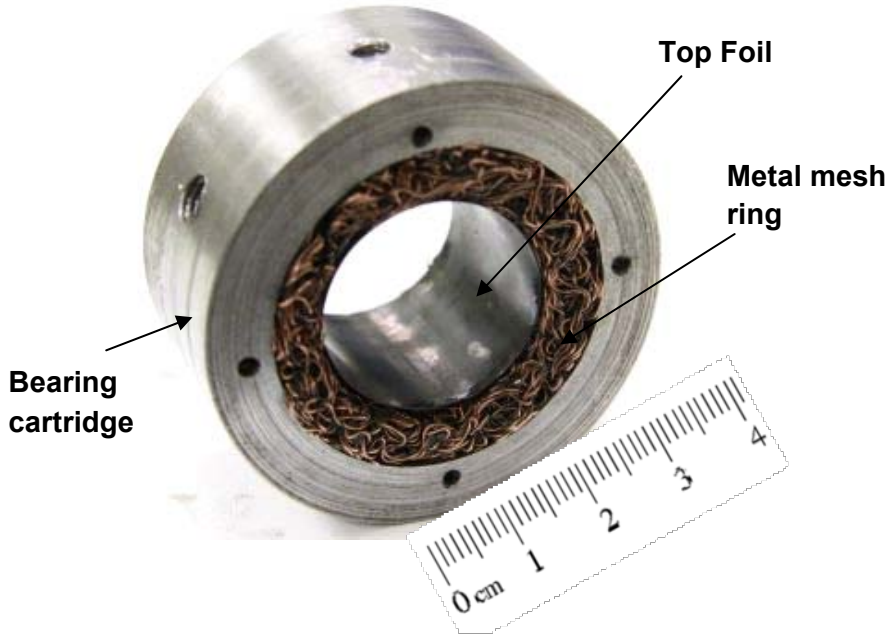

Fig. 6 Photograph of a metal mesh foil bearing manufactured at TAMU

The top foil is made from a cold rolled steel strip (Chrome-Nickel alloy, Rockwell 40/45) with significant resilience to deformation. The steel strip is first heat treated in a die at a temperature of 927° C and then allowed to cool for ~ 10 hours. Further, a tempering process at ~ 400 ° C toughens the formed top foil. The heat treatment process follows the recommendations in Ref. [14] that details the heat treatment processes typically employed in the manufacturing of top foils in commercial bearings.

Table 1. Description of metal mesh foil bearing components

	Description	Role
Bearing Cartridge	Stainless steel cylindrical ring	Cartridge holding metal mesh ring and smooth top foil.
Metal mesh ring (MM)	Ring shaped compressed woven wire mesh	Soft material support provides structural stiffness and energy dissipation
Smooth top Foil	Thin Stainless steel sheet, curved and preformed, with one end affixed to the metal mesh ring and the other end free.	A hydrodynamic film pressure builds up within the gap between the rotating shaft and the top foil.

Figure 7 displays a schematic representation of a cross sectional view of the test MMFB and illustrates the installation of the smooth arcuate top foil inside the metal mesh ring. One end of the top foil has two identical shaped tabs that are bent and fit into the two apertures inside the ring shaped metal mesh during assembly. After affixing the top foil into the metal mesh, the assembly is inserted into the bearing cartridge to complete the construction of the MMFB [6]. A thin and uniform solid lubricant coating of MoS_2 is applied on the top foil inner surface to protect it from excessive wear due to frictional contact with the rotating journal. Table 2 displays the dimensions of the MMFB with the metal mesh ring inner diameter of 28.30 mm and axial length of 28.05 mm. Cooper wire with a diameter of 0.30 mm comprises of a metal mesh ring with a compactness of 20%. The compactness (wire density) of the metal mesh determines its physical (equivalent) properties [3]. Stainless steel top foil thickness is 0.127 mm. The total mass of MMFB including a torque arm (see Fig. 8) is ~ 0.363 kg.

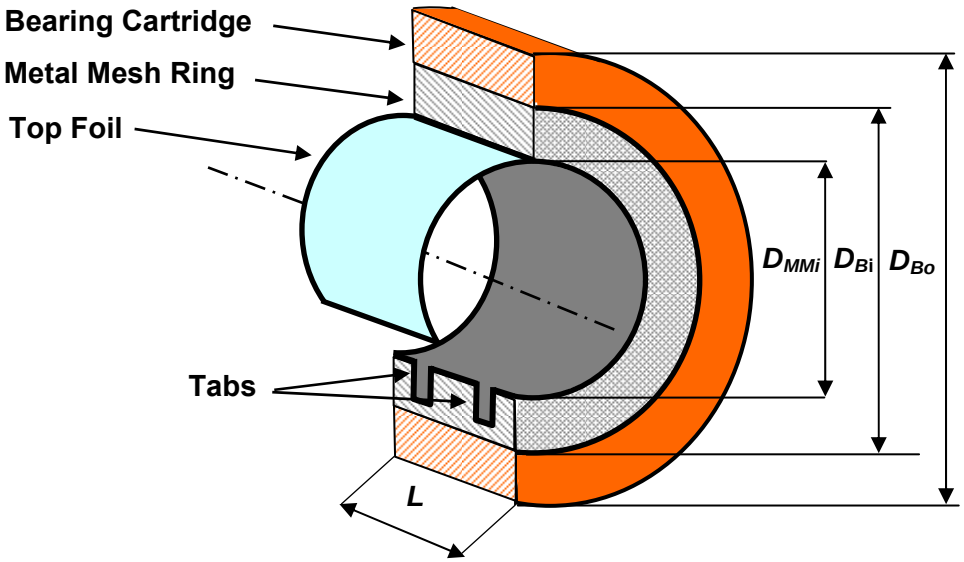

Fig. 7 Schematic representation of cut view of the MMFB

Table 2. Nominal dimensions and material specifications for test MMFB

Parameter name and physical dimension	Magnitude
Bearing cartridge outer diameter, D_{Bo} (mm)	58.15 ± 0.02
Bearing cartridge inner diameter, D_{Bi} (mm)	42.10 ± 0.02
Bearing axial length, L (mm)	28.05 ± 0.02
Metal mesh outer diameter, D_{MMo} (mm)	42.10 ± 0.02
Metal mesh inner diameter, D_{MMi} (mm)	28.30 ± 0.02
Metal mesh mass, M_m (kg)	0.0391
Metal mesh density, ρ_{MM} (%)[1]	20
Top foil thickness, T_{tf} (mm)	0.127
Wire diameter, D_W (mm)	0.30
Copper Young modulus, E (GPa), at 21 ºC [18]	114
Copper Poisson ratio, υ [19]	0.33
Bearing mass (cartridge + mesh + foil + torque arm), M (kg)	0.363

Uncertainty in mass measurement = ±0.0001 kg

[1] Manufacturers define the density of metal mesh as the ratio of the ring mass to its volume times the metal material density.

EXPERIMENTAL FACILITY

Figure 8 shows a photograph of the test rig with a ball bearing supported turbocharger (TC) turbine driving the system to a maximum speed of 120 krpm. The compressor impeller and volute of the original TC are removed to expose the overhanging shaft. A journal of diameter 28 mm and length 55 mm is press fitted on the TC shaft end and fastened with a nut. The journal is balanced in-place using correction masses inserted at eight equally spaced threaded holes on the journal front face. The MMFB slides on the journal and remains afloat when the journal starts rotating. A torque arm attached to the bearing prevents its rotation.

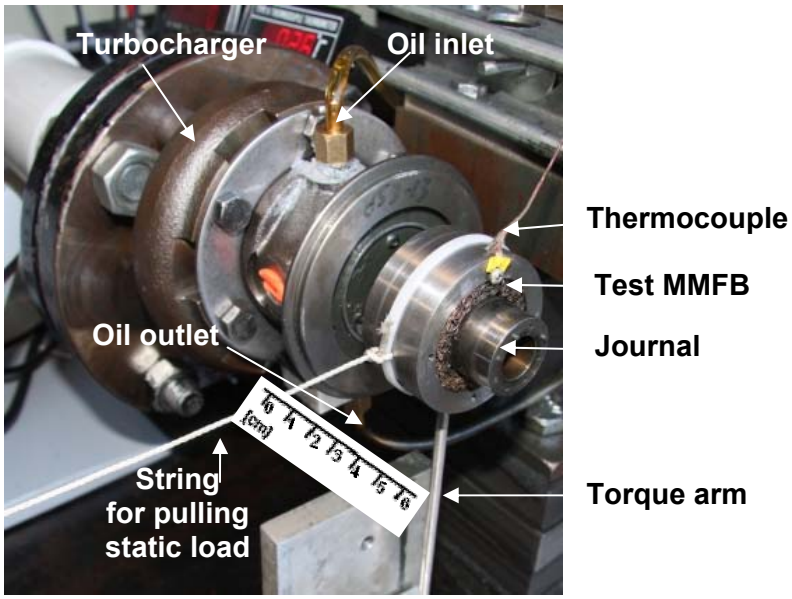

Fig. 8 Photograph of test rig with metal mesh foil bearing mounted on journal (28 mm diameter and 55 mm length

Figure 9 shows a schematic front view of the test bearing, journal, and the devices for measurement of torque, applied load and temperature. Once the journal starts rotating, the torque arm applies a force on the soft spring (0.88 kN/m), and the spring reaction force balances the drag moment acting on the bearing. An eddy current sensor records the lateral displacement of the torque arm. The rubber band shown gives a slight preload and prevents axial motions of the test bearing.

Static (horizontal) loads are applied on the bearing by pulling a string (flexible) connected to the bearing, using a positioning table. A dynamometer (± 0.2 N) affixed to the linear positioning table measures the applied load. As the positioning table moves toward left, as illustrated in

Figure 9, the string applies a horizontal load on the bearing floating on the shaft. Note that the string, loosely wound around the bearing circumference (at its axial mid-plane) does not prevent the bearing rotation, thus facilitating seamless torque measurement. Incidentally, note that the weight of the bearing assembly is 3.5 N. A K-type thermocouple affixed at one of the bearing ends measures the top foil temperature (± 0.5 °C). An infrared tachometer, mounted within the safety structure, measures the turbine tip speed with ± 0.0015 % accuracy.

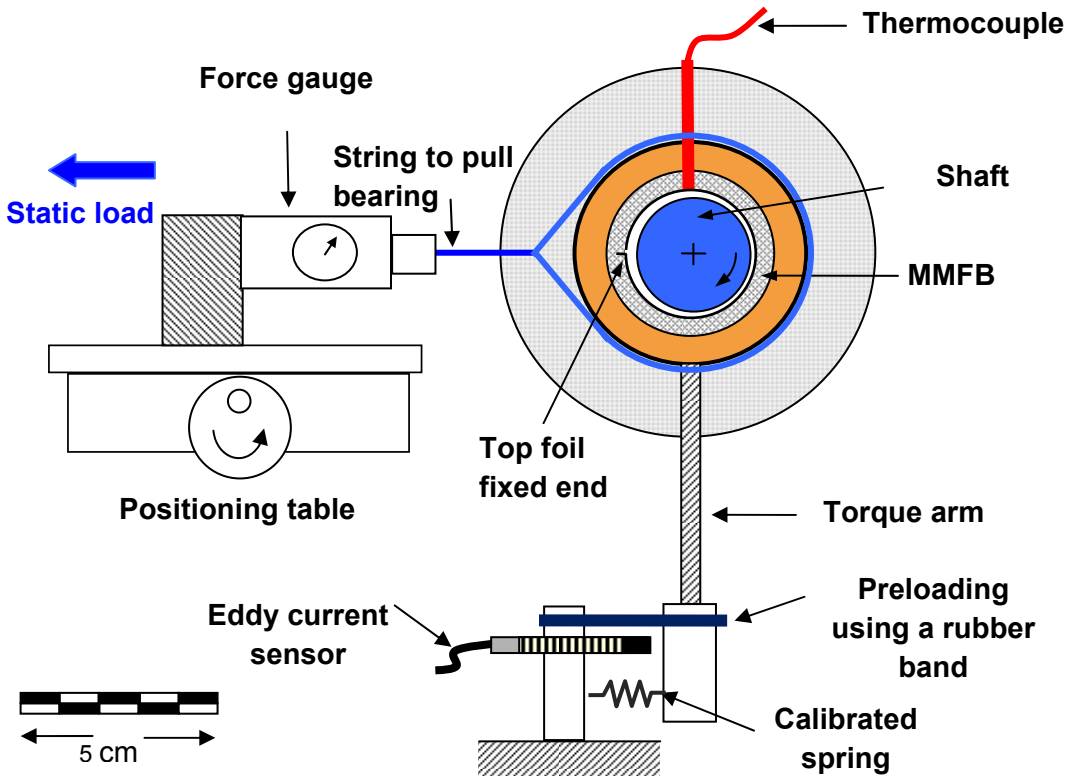

Fig. 9 Schematic view of MMFB, rotating journal, and instrumentation for static (pull) load and torque measurements

A pressure regulator adjusts the supply air pressure [8.1 bar (120 psig) max.] into the turbine inlet. A ball valve throttles the inlet air and the exhaust air is routed from the test cell to the outside environment. The gradual increase of the inlet air into the turbine accelerates the rotor to a certain steady state speed. Further, depending on the test type, either the inlet air is suddenly cut or gradually reduced (stepwise), the rotor speed decreases until it stops rotating.

The torque arm is later removed and two eddy current sensors and two miniature piezoelectric accelerometers (each weighing 5.1 g), as shown in Figure 10, are affixed to the test

bearing along orthogonal directions for measuring the bearing motion while the shaft (journal) spins.

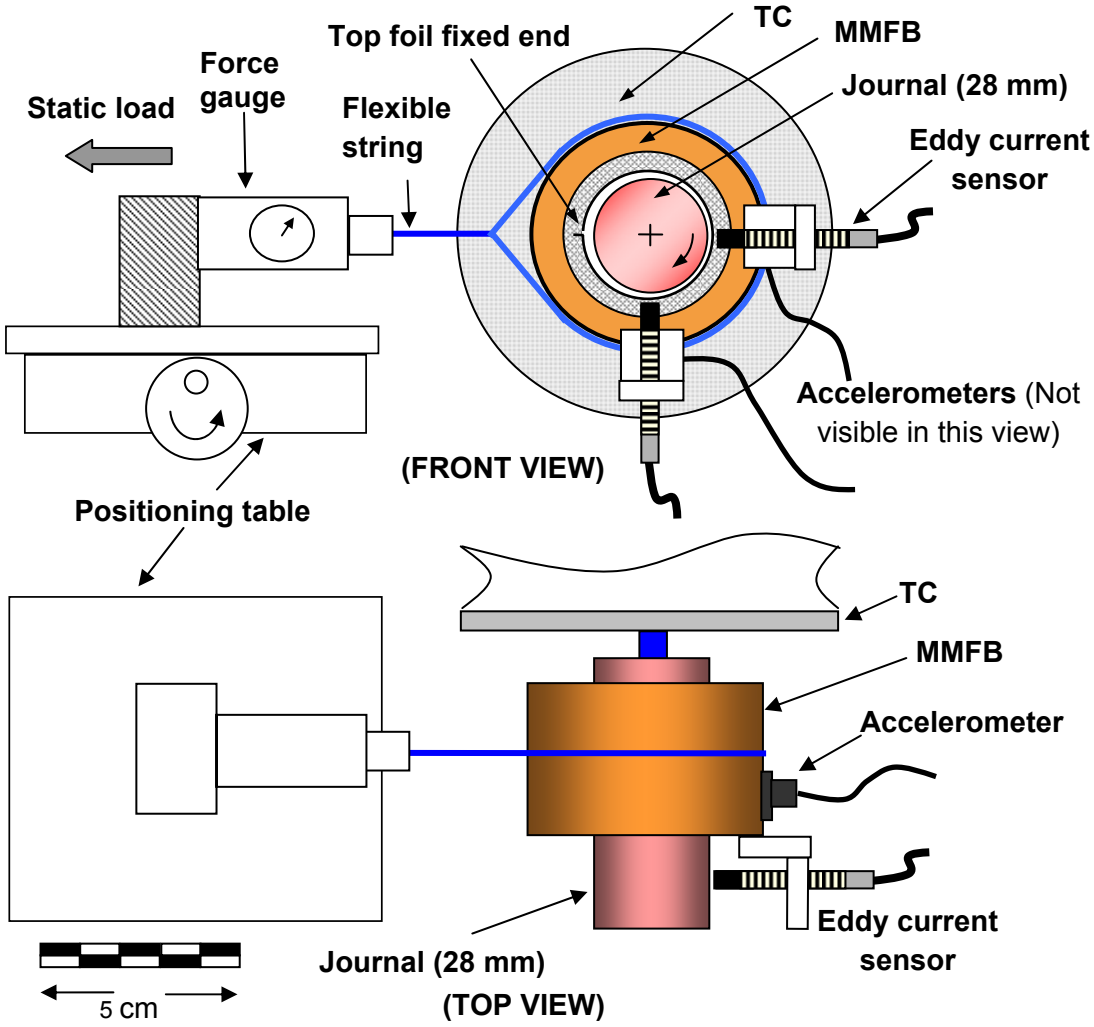

Fig. 10 Schematic views of MMFB mounted on shaft of turbocharger drive system. Sensors for measuring bearing accelerations and displacements relative to shaft (horizontal and vertical directions) shown

IV. MEASUREMENT OF DRAG TORQUE, LIFT-OFF SPEED, AND TOP FOIL TEMPERATURE IN A METAL MESH FOIL BEARING

MEASUREMENT OF BEARING DRAG TORQUE

The air inlet valve is controlled to accelerate the TC shaft from rest, maintain it at a steady speed, and then decelerate it to rest as the air valve is closed. Figure 11 shows the journal speed and bearing drag torque versus time during a lift-off test cycle with an applied static (pull) load of 17.8 N (4 lb). The rotor accelerates beyond the bearing lift of speed (~ 28 krpm) to a steady speed of 65 kprm, and then decelerated to rest. As the rotor starts to spin, rubbing between the journal and top foil surfaces generate a sharp peak in bearing torque (~ 110 N-mm). Once the journal starts rotating, the torque falls rapidly. Further, the bearing operates in a mixed lubrication regime with partial asperity contacts, until the thin air film completely separates the two surfaces. The airborne journal, at a steady speed of 65 kprm, offers a significantly smaller drag torque of ~ 3.2 N-mm, i.e. 3% of the peak (break-up) torque. While decelerating to rest, the journal comes into physical contact with the top foil and causes a sharp peak in the drag torque (80 N-mm).

The lift-off shut-down test cycle is again conducted with a step wise change in the rotating speed. Figure 12 shows the rotor speed and bearing drag torque versus time with an applied static load of 8.9 N (2 lb). Note that the (horizontal) direction of the static pulling load (*WS*) is 90° away from that of the bearing dead weight (*WD*=3.5 N). Hence, the total static load acting on the MMFB is $W = \sqrt{W_S^2 + W_D^2}$ [2].The opening of the valve instantly brings the rotor to 65 krpm, overcoming a dry friction torque, due to rubbing with the top foil, of 57 N-mm. Once airborne, the viscous drag torque, between the air film and the top foil, is only 2.5 N-mm. Next, after every 20 s, the air inlet valve to the turbine is closed a little more, to reduce the rotor speed in a stepwise manner. The drag torque decreases with journal speed, to 2.4 N-mm at 50 krpm, to 2.0 N-mm at 37 krpm, to 1.7 N-mm at 24 krpm, respectively. Further reduction in the rotor speed evidences an increase in drag torque. The drag torque peaks to 45 N-mm just before the rotor comes to rest.

[2] Total static load is 9.6 N, 18.2 N, 26.9 N, and 35.8 N for the applied (horizontal) static loads of 8.9 N, 17.8 N, 26.7 N, and 35.6 N, respectively.

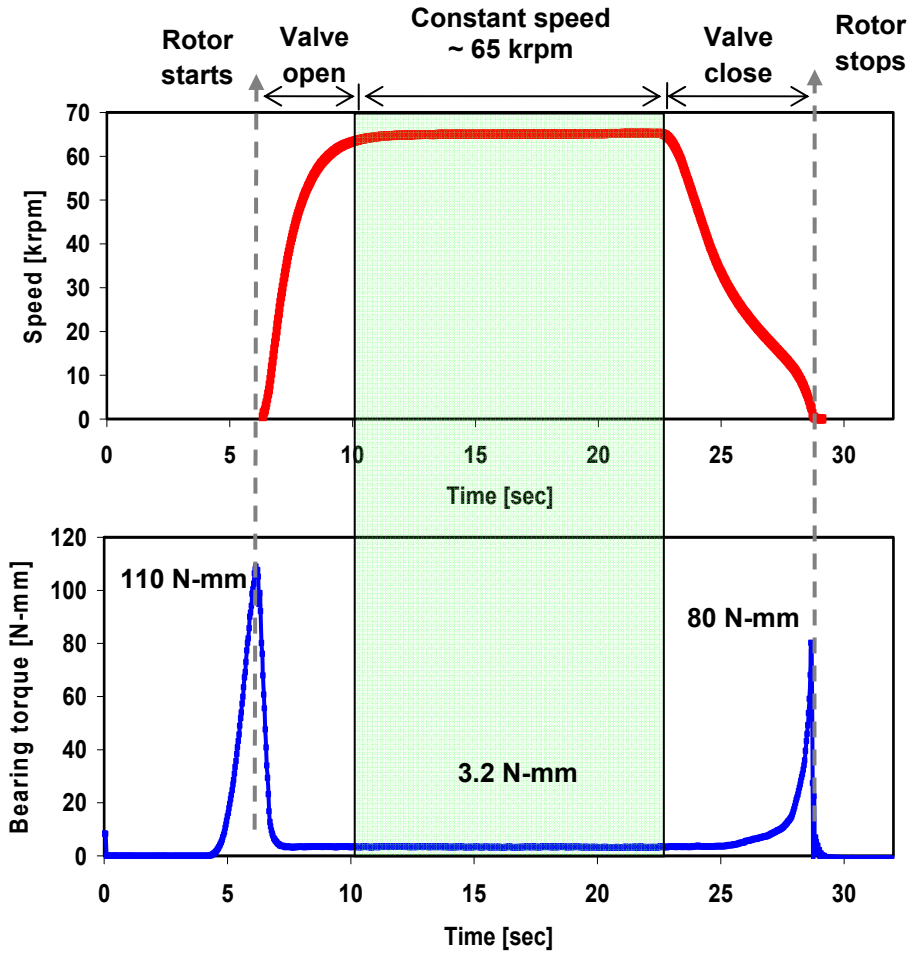

Fig. 11 Rotor speed and bearing torque versus time during a lift-off test cycle for applied static load of 17.8 N (4 lb). Manual speed-up to 65 krpm, operation at a constant rotor speed of 65 krpm, and deceleration to rest

Bearing lift-off tests with stepwise variation in rotor speed, as shown in Figure 12, are repeated for increasing static loads (18.2 N, 26.9 N, and 35.8 N). Figure 13 depicts the steady state (viscous) drag torque while the bearing is airborne. The bearing drag torque increases with increasing rotor speed and static loads. For static loads larger than 18.2 N, the rotor lift-off speeds are above 35 krpm.

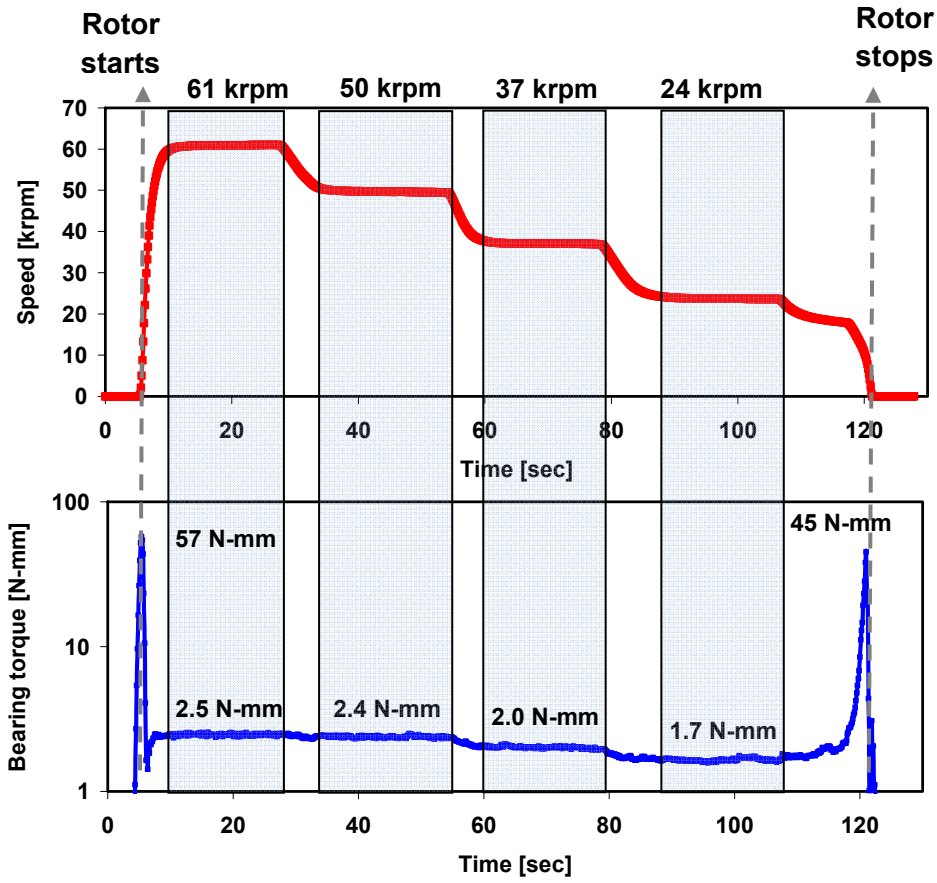

Fig. 12 Rotor speed and bearing torque versus time during a lift-off test cycle with scheduled variations in speed. Applied static load of 8.9 N (2 lb). Manual speed-up to 61 krpm, operation at fixed rotor speeds of 60, 50, 37, 24 krpm and deceleration to rest

Figure 14 shows the friction coefficient (*f*) derived from the data in Figure 13. Recall that $f = Torque / (WR)$ with R = ½D = 14 mm is the journal radius. As expected, the friction coefficient is nearly proportional to the rotor speed. However, the friction coefficient decreases as the static load increases. The highest friction factor of 0.018 is recorded for the smallest load (8.9 N) at the top speed of 61 krpm. The friction coefficient due to the hydrodynamic viscous drag is quite small. Hence, the MMFB when airborne offers negligible power losses.

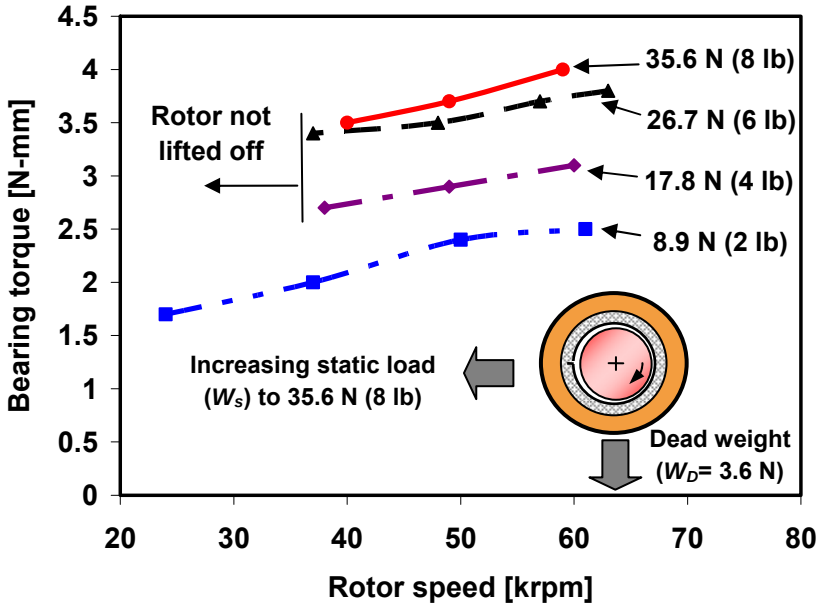

Fig. 13 Bearing viscous drag torque versus rotor speed for increasing static loads. MMFB airborne

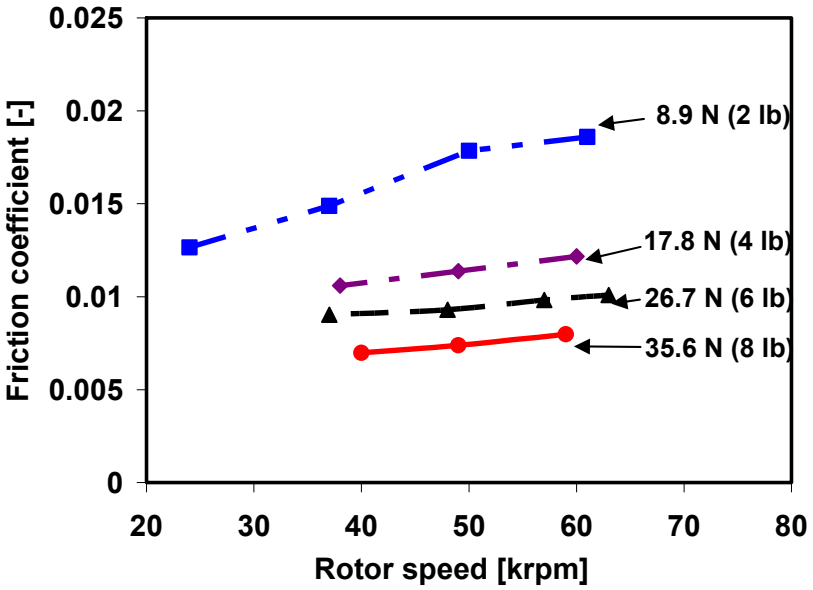

Fig. 14 MMFB friction coefficient *f* versus rotor speed for increasing static loads. Steady state operation with bearing airborne

Figure 15 displays the bearing break away torque versus static load measured during (four) rotor speed-up tests to ~ 60 krpm. The largest dry friction induced torque is observed when the rotor begins to spin. After the series of rotor liftoff tests, a post-inspection of the top foil surface showed its protective MoS_2 layer had disappeared. The top foil surface is sprayed again with the

solid lubricant, and the bearing break away torque measured while rotating the journal manually. Figure 15, showing these measurements, clearly depicts that the recoated top foil surface reduces the drag torque, for instance by ~30 % for the highest static load of 35.8 N.

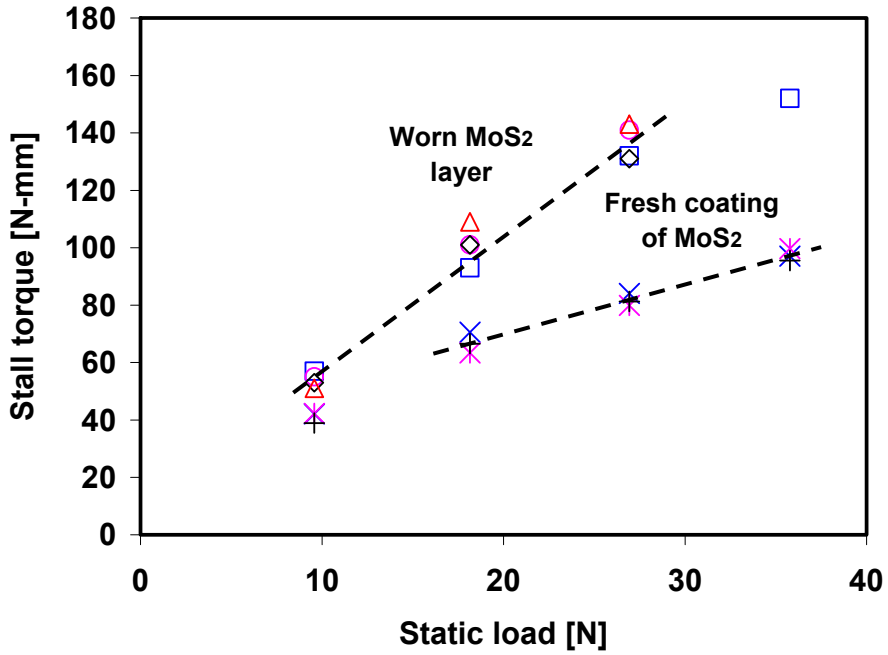

Fig. 15 MMFB break away torque versus static load. Measurements from rotor speed start up tests to 60 krpm and post-test with (fresh) MoS_2 layer deposited on top foil

Figure 16 depicts the bearing friction coefficient $f = Torque/(WR)$ estimated from the measurements shown in Figure 15. This friction coefficient represents the rubbing contact (dry frictional sliding) between the rotor and the top foil surface. The estimated value of f decreases from ~0.4 to ~ 0.37, with an increase in the static load from 9.6 N to 35.8 N, for the top foil with a worn layer of MoS_2. These friction coefficient magnitudes are typical for metal to metal contact. After spraying the top foil with a new sacrificial layer of MoS_2, the dry friction coefficient ranges from ~0.3 to 0.2 as the static load increases from 9.6 N to 35.8 N. The experimental results imply the need of adequate and enduring solid lubricants to reduce MMFB drag torque during the rotor start up (and shut down.

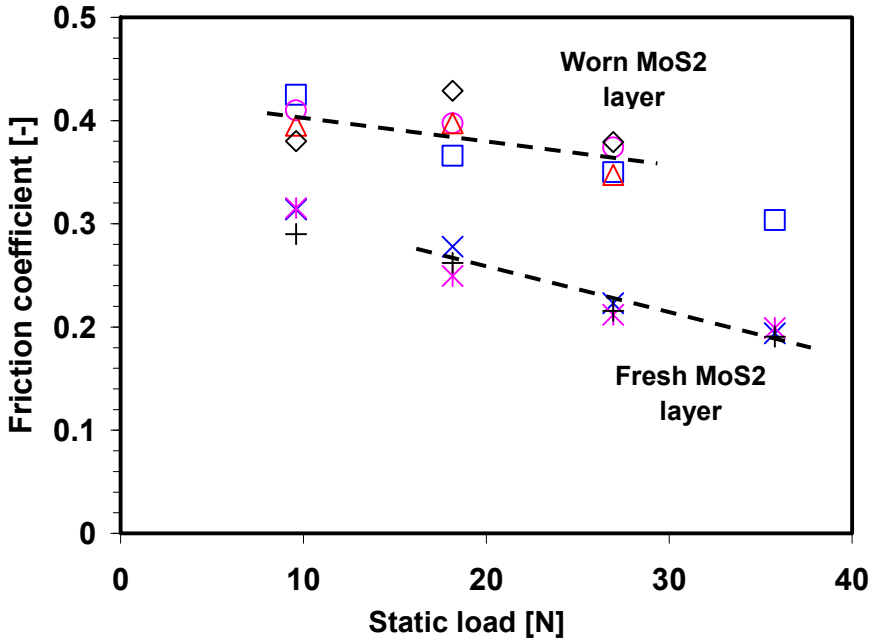

Fig. 16 Dry-friction coefficient of MMFB versus static loads. Measurements from rotor speed start up tests to 60 krpm and post-test with (fresh) MoS_2 layer deposited on top foil

Figure 17 shows the bearing drag torque versus rotor speed, during rotor speedup, for increasing static loads of 9.6 N, 18.2 N, 26.9 N and 35.8 N. Note that the uncertainty in drag torque is ± 0.35N-mm for drag torque < 10 N-mm. For each static load, as the rotor speed increases, initially the bearing drag torque decreases quickly and, when the journal is airborne, increases gradually with rotor speed. The lowest drag torque provides the rotor lift off speed. Note that for operation at 60 krpm, the measured drag torque is nearly identical to those recorded under steady journal speed, see Figure 13. Figure 18 show that the friction coefficient f changes only slightly with rotor speed after the rotor is airborne, i.e. once the MMFB operates with a hydrodynamic film. The identified f is the lowest for the largest applied load of 35.8 N.

Owing to the very low friction coefficient, f ~0.01 to 0.02 (when the bearing is airborne), the drag power losses in the bearing are rather small. For example, at 60 krpm and the highest static load, the estimated power loss, $P = T_{orque} \times \Omega \sim 4$ N-mm x 60000 (π/30) = 25.1 W.

The rotor lift-off speed, as shown in Figure 19, is proportional to the static load imposed on the bearing. Once the shaft starts spinning, the bearing drag torque rises to a peak; then at a certain threshold speed when the bearing is airborne, the torque suddenly drops and remains at this small magnitude as long as there is an air film. The rotational speed beyond which the bearing operates with a significantly smaller drag torque, in comparison to the large startup

rubbing torque, is herby termed the lift off speed, as shown in Figure 17. Note that the rotor lift-off speed also indicates the lowest rotor speed to support a static load without rubbing or contact between the shaft and top foil. Appendix B shows the uncertainty analysis for torque estimations.

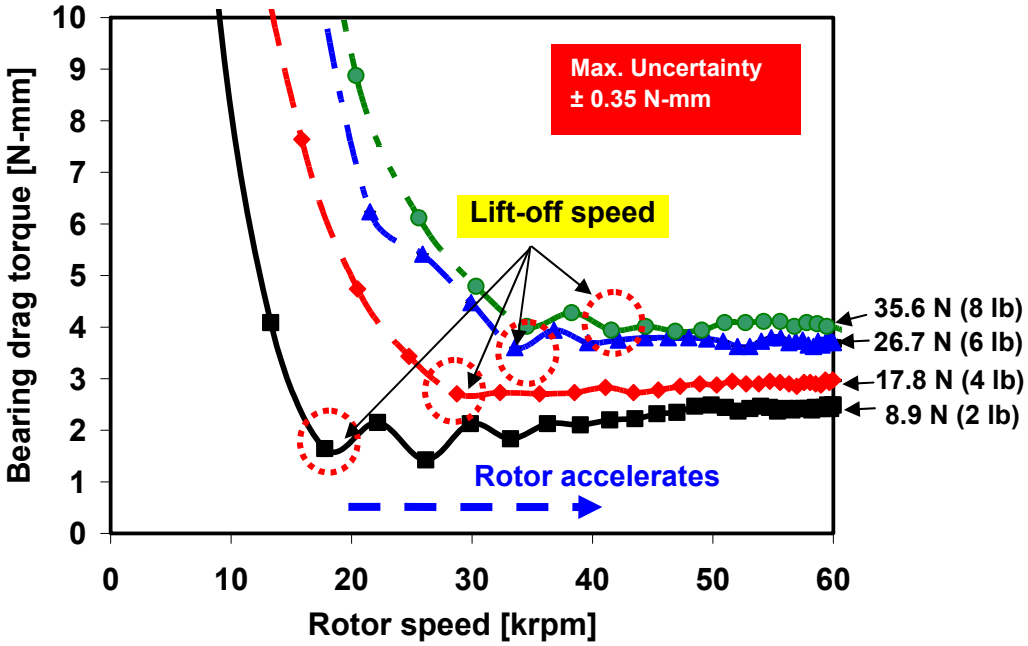

Fig. 17 Bearing drag torque versus rotor speed for increasing static loads. Measurement during rotor speed-up tests

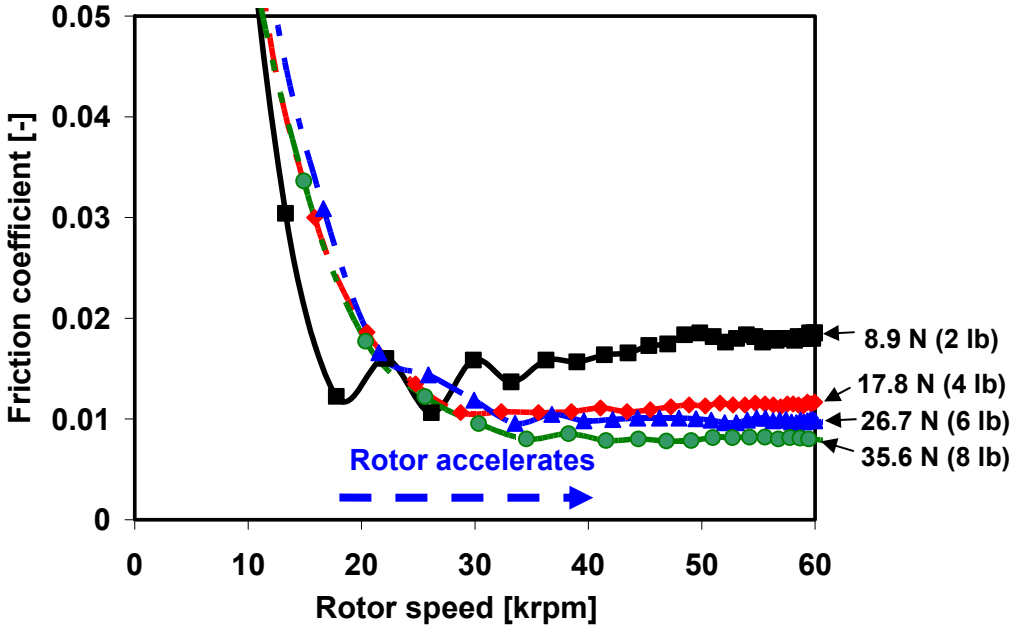

Fig. 18 Friction coefficient versus rotor speed for increasing static loads. Measurement during rotor speed-up tests

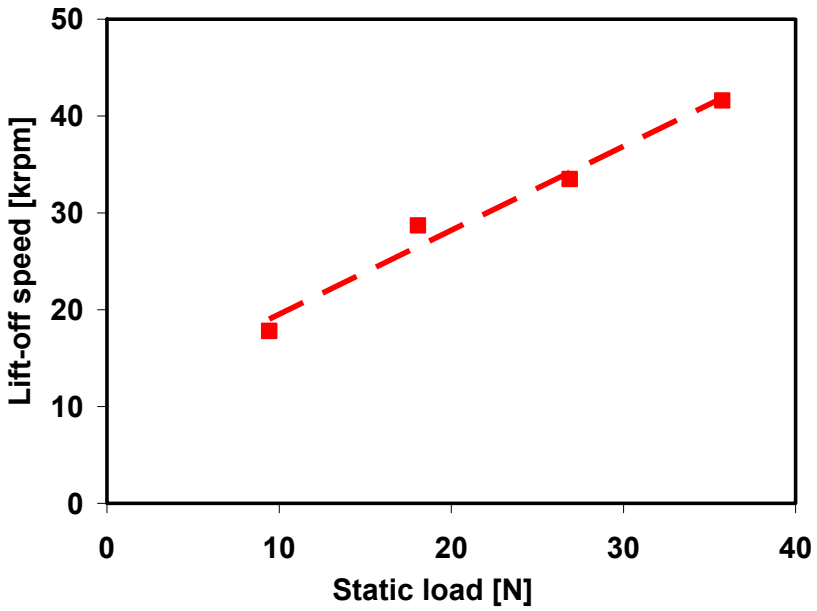

Fig. 19 MMFB: Rotor lift-off speed versus static load from smallest drag torque (see Fig.17)

MEASUREMENT OF TOP FOIL TEMPERATURE

Figure 20 shows the bearing temperature rise versus rotor speed for increasing static loads. The temperature is measured at the free end of the bearing with a thermocouple glued on the back surface of the top foil. The temperatures shown correspond to steady state values after continuous operation, no less than15 minutes, at the specified load and rotor speed. The elapsed time for the entire test is four hours. In general, the bearing temperature increases linearly with rotor speed and applied static load, as also reported in Ref. [20]. At the two lowest rotor speeds, the measured temperatures are identical uncertainty ± 0.5 °C). In general, the temperature increase is quite modest for the test since the specific loads applied are rather small, i.e. W_{max}/LD= 45.5 kN/m^2 (6.6 psi)

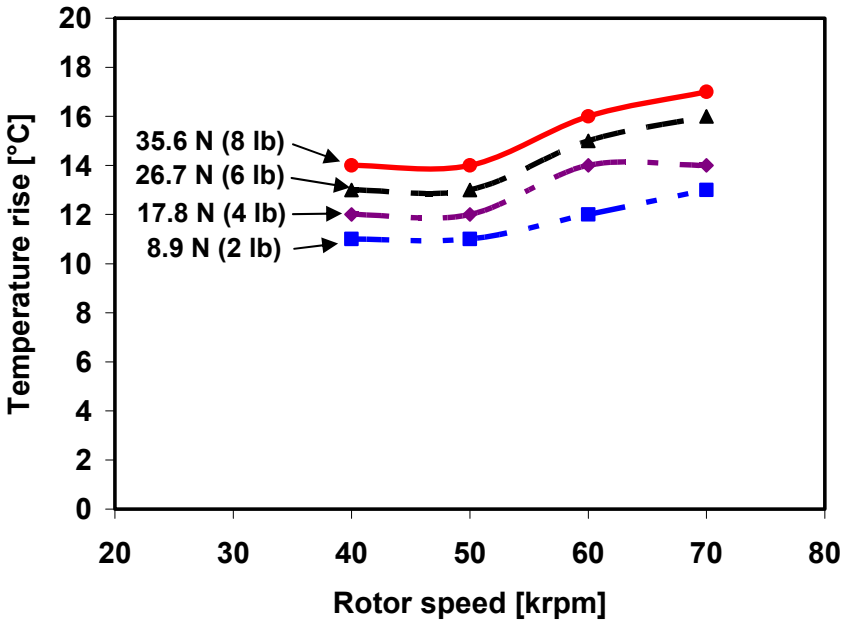

Fig. 20 Bearing temperature rise versus rotor speed for airborne operation with increasing static loads. Estimation at steady state rotor speeds (after 15 min. for each condition). Ambient temperature at 21 °C

V. CONCLUSIONS

Metal mesh foil bearings (MMFBs) offer promise as a reliable support in oil-free high speed rotating machinery. MMFBs provide a tunable resilient support with large (material) damping. Most importantly, the MMFB configuration is simple and of little cost since it uses commercially available materials. Note that metal mesh ring structural properties can be changed by modifying its geometrical dimensions and compactness, thus promoting the scalability of this bearing technology.

The report presents the measurement of drag torque, rotor lift-off speed, and operating temperature of a test MMFB mounted on a turbocharger air turbine driven test rig. The measurements aim to characterize the static load performance of the MMFB over broad ranges of rotor speed and static loads. The measurements show that the bearing break-away torque during rotor speed start-up increases with increasing static loads. This dry-friction torque, typical of metal to metal contact, is reduced by application of a sacrificial layer of MoS2. During rotor airborne (hydrodynamic) operation, the bearing drag torque increases with the static load and rotor speed. However, the friction coefficient is rather small (< 0.010) denoting negligible

power losses. The rotor lift-off speed, estimated at the lowest drag torque, increases linearly with static load. The test bearing steady state temperature is proportional to rotor speed and increases with the applied static load. The experimental results provide a comprehensive database on the static load performance of the simple and low cost prototype MMFB for increasing rotor speed and temperature. The measurements demonstrate the reliable performance of a MMFB for an oil-free application and pave the way for further developments.

MMFB structural stiffness and damping coefficients are identified, for the range of frequencies 0-125 Hz, from impact load tests (See Appendix C). In these tests, the shaft does not spin and the only load is due to the bearing weight. The bearing response shows a system with large damping. The identified structural static stiffness is ~0.1 MN/m. The frequency dependent stiffness gradually increases with frequency. The equivalent viscous damping coefficient decreases from ~400 Ns/m to ~200 Ns/m as the frequency increases from 10 to 125 Hz. Further experiments to determine the bearing force coefficients while the shaft rotates are planned.

CIATEQ A.C., a TRC member, donated two aluminum foam bearings; their viability for use in high speed turbomachinery is not recommended due to their large stiffness and delicate integrity of the metal foam.

REFERENCES

[1] Agrawal, G., 1997, "Foil Air/Gas Bearing Technology – an Overview," ASME Paper No. 97-GT-347.

[2] Valco, M.J., and DellaCorte, C., 2002, "Emerging Oil-Free Turbomachinery Technology for Military Propulsion and Power Applications," *Proc. Of 23rd U.S. Army Science Conf.* Ft. Lauderdale, FL, Dec. 2-5.

[3] Al-Khateeb, E. M., 2002, "Design, Modeling and Experimental Investigation of Wire Mesh Vibration Dampers," PhD. Thesis, Texas A&M Univ. College Station, TX.

[4] Lee, Y. B., Kim, C. H., Jo, J. H., and Ryu, K., 2006, "Air Foil Bearing Having a Porous Foil," International Patent No. WO 2006/043736 A1.

[5] Zarzour, M. and Vance, J., 2000, "Experimental Evaluation of a Metal Mesh Bearing Damper," ASME J. Eng. Gas Turbines Power, **122**(2), pp. 326-329.

[6] San Andrés, L., Kim, T. H., Chirathadam, T. A., and Martinez, A., 2008, "Measurement of Structural Stiffness and Damping in a Metal Mesh Foil Bearing and Development of a Test

Rig for Gas Foil Bearings," Technical Report TRC-B&C-5-08, Texas A&M Univ., College Station, TX.

[7] Pinkus, O., 1987, "The Reynolds Centennial: A Brief History of the Theory of Lubrication," ASME J. Trib., **109**, pp. 1-20.

[8] Blok, H. and van Rossum, J. J., 1953, "The Foil Bearing – A New Departure in Hydrodynamic Lubrication," Lub. Eng., **9**(6), pp. 316-320

[9] DellaCorte, C., and Valco, M.J., 2000, "Load Capacity Estimation of Foil Air Journal Bearings for Oil-Free Turbomachinery Applications," NASA/TM-2000-209782.

[10] DellaCorte, C., 1997, "A New Foil Air Bearing Test Rig for use to 700° C and 70,000 rpm," NASA/TM-107405.

[11] DellaCorte, C., Lukaszewics, V., Valco, M.J., Radil, K.C., and Heshmat, H., 2000, "Performance and Durability of High Temperature Foil Air Bearings for Oil-Free Turbomachinery," NASA/TM-2000-209187/REV1.

[12] Radil, K., Howard, S., and Dykas, B., 2002, "The Role of Radial Clearance on the Performance of Foil Air Bearings," NASA/TM-2002-211705.

[13] DellaCorte, C., Radil, K. C., Bruckner, R. J., and Howard, S. A., 2008, " Design, Fabrication, and Performance of Open Source Generation I and II Compliant Hydrodynamic Gas Foil Bearings," Tribol. Transactions, **51**, pp. 254-264.

[14] Peng, Z.-C., and Khonsari, M. M., 2004, "On the Limiting Load-Carrying Capacity of Foil Bearings," ASME J. Tribol., **126**, pp. 817-818.

[15] Kim, T.H., and L. San Andrés, 2006, "Limits for High Speed Operation of Gas Foil Bearings," ASME J. Tribol., **128**, pp. 670-673.

[16] DellaCorte, C., Zaldana, A., and Radil, K., 2003, "A System Approach to the Solid Lubrication of Foil Air Bearing for Oil-Free Turbomachinery," ASME J. Tribol., **126**(1), pp. 200-207.

[17] Jahanmir, S., Heshmat, H., and Heshmat, C., 2009, "Evaluation of DLC Coatings for High-Temperature Foil Bearing Applications," ASME J. Tribology, **131**, pp. 011301-(1-11).

[18] Dodge, H.L., 1913, "The Physical Review," American Institute of Physics, pp. 439.

[19] Boyd, J. E., 1917, *Strength of Materials*, McGraw-Hill Book Company, New York, pp.

[20] San Andrés, L., Kim, T.H., Ryu, K., Chirathadam, T. A.,Jarrett, C., Hagen, K., Martinez, A., Rice, B., Niedbalski, N., Hung, W., and Johnson, M., "Gas Bearing Technology for Oil-Free

Microturbomachinery – Research Experience for Undergraduate (REU) Program at Texas A&M University," ASME Paper No. GT2009-59920

APPENDIX A. CALIBRATION OF EDDY CURRENT SENSOR AND SPRING CONSTANT

Figures A.1 and A.2 display the calibration curves for a mechanical spring (torque measurement) and an eddy current sensor (Aluminum target). A dynamometer applies a force on the steel spring and the eddy current sensor measures the corresponding deflection. The estimated spring constant is 879.5 N/m. The gain of the eddy current sensor for the Aluminum target, 13.446 V/mm, is estimated using the displacement reading from a positioning table digital readout and the corresponding eddy current sensor voltage due to the aluminum target displacement.

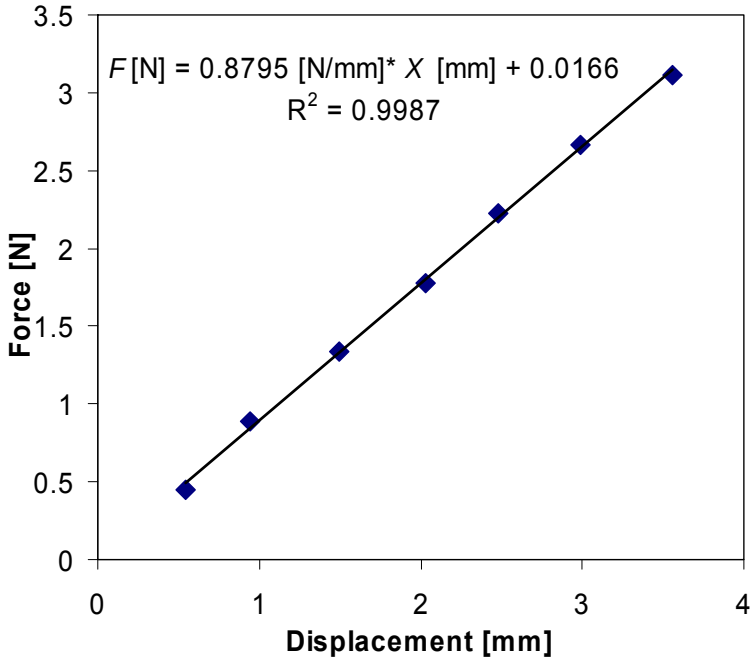

Fig. A.1 Force versus displacement (Calibration of spring for torque measurement)

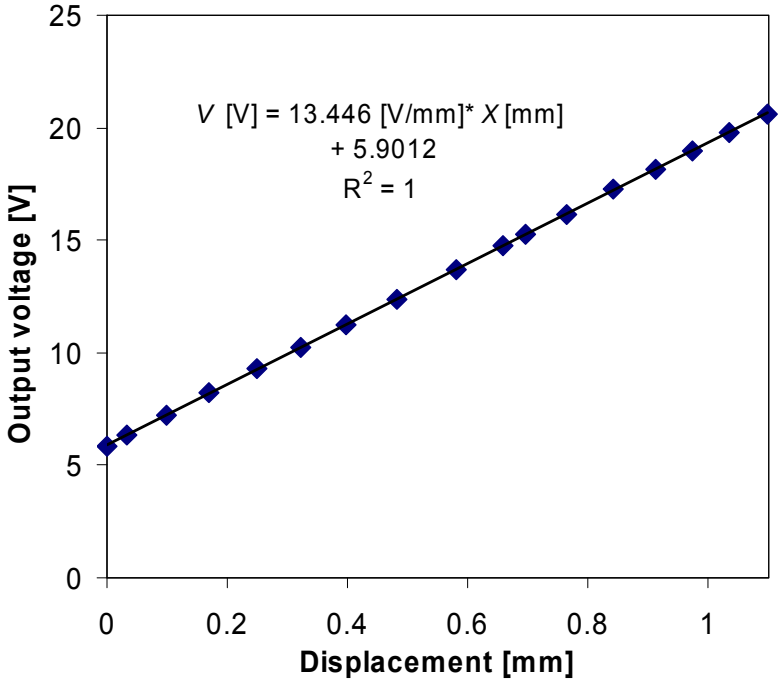

Fig. A.2 Calibration of Eddy Current Sensor (3300 XL) for Aluminum target

APPENDIX B. UNCERTAINTY ANALYSIS

EDDY CURRENT SENSOR CALIBRATION

The proximity sensor calibration uses displacement reading from a positioning table digital readout (U_d = ± 0.0005 mm) and a voltmeter (U_v= ± 0.005 V). The eddy current proximity sensor gain follows the relationship

$$G = \frac{\Delta D}{\Delta V_{fit}} \tag{B.1}$$

where ΔD is the change in displacement for a change in voltage, $\Delta V_{fit.}$, resulting from the linear fit. The general equation for computing the uncertainty of parameters for a typical expression, $r = f(x_1, x_2, \ldots x_n s)$, is defined as

$$U_r = \sqrt{(\frac{\partial r}{\partial x_1} U_{x_1})^2 + (\frac{\partial r}{\partial x_1} U_{x_2})^2 + \ldots + (\frac{\partial r}{\partial x_n} U_{x_n})^2} \tag{B.2}$$

The uncertainty of expression B.1, using equation B.2 becomes

$$(\frac{U_G}{G})^2 = (\frac{\partial G}{\partial D}\frac{U_D}{D})^2 + (\frac{\partial G}{\partial V_{fit}}\frac{U_{fit}}{G})^2 = (\frac{1}{\Delta D}\frac{U_D}{})^2 + (\frac{1}{\Delta V_{fit}}\frac{U_{V_{fit}}}{})^2 \tag{B.3}$$

where ΔD and ΔV_{fit} are the range of experimental values and $U_{V_{fit}}$ is computed from the uncertainty of the voltmeter and the uncertainty of the curve fit as described

$$U_{V_{fit}} = \sqrt{(U_{fit})^2 + (U_V)^2} \tag{B.4}$$

Hence, G =13.44 ± 0.007 V/mm

CALIBRATION OF SPRING CONSTANT

The spring[3] constant calibration uses displacement reading from a positioning table digital readout (U_d = ±0.0005 mm) and a force gauge (U_f = ± 0.2 N). The spring constant follows the relationship

$$K = \frac{\Delta F}{\Delta D_{fit}} \tag{B.5}$$

[3] For measurement of drag torque

The uncertainty of expression B.5, using equation B.2 becomes

$$(\frac{U_K}{K})^2 = (\frac{\partial K}{\partial F}\frac{U_F}{F})^2 + (\frac{\partial K}{\partial D_{fit}}\frac{U_{fit}}{K})^2 = (\frac{1}{\Delta F}\frac{U_F}{})^2 + (\frac{1}{\Delta D_{fit}}\frac{U_{D_{fit}}}{})^2 \quad \text{(B.6)}$$

Where ΔF and ΔD_{fit} are the range of experimental values and $U_{D_{fit}}$ is computed from the uncertainty of the displacement measurement and the uncertainty of the curve fit as described

$$U_{D_{fit}} = \sqrt{(U_{fit})^2 + (U_D)^2} \quad \text{(B.7)}$$

Thus, K = 0.88 ± 0.03 N/mm

TORQUE MEASUREMENT

The torque measurement follows the relationship

$$T = V\,G\,K\,L \quad \text{(B.8)}$$

where, T is the bearing torque, V the voltmeter reading, G the Eddy current sensor gain, K the spring constant, and L the torque arm length. The uncertainty of expression B.8, using equation B.2 becomes

$$(\frac{U_T}{T})^2 = (\frac{U_V}{V})^2 + (\frac{U_G}{G})^2 + (\frac{U_K}{K})^2 + (\frac{U_L}{L})^2 \quad \text{(B.9)}$$

The uncertainty in the measurement of torque of 10 Nmm is ± 0.35 Nmm using eqn. (B.9)

APPENDIX C. IDENTIFICATION OF MMFB STIFFNESS AND DAMPING COEFFICIENTS FROM IMPACT LOAD TESTS

MODEL OF THE TEST BEARING

Figure C.1 shows a representation of the bearing force coefficients and the impact forces exerted on the test bearing. Recall that the bearing floats atop the rotating shaft or journal, and it rests on the journal while the journal is not rotating.

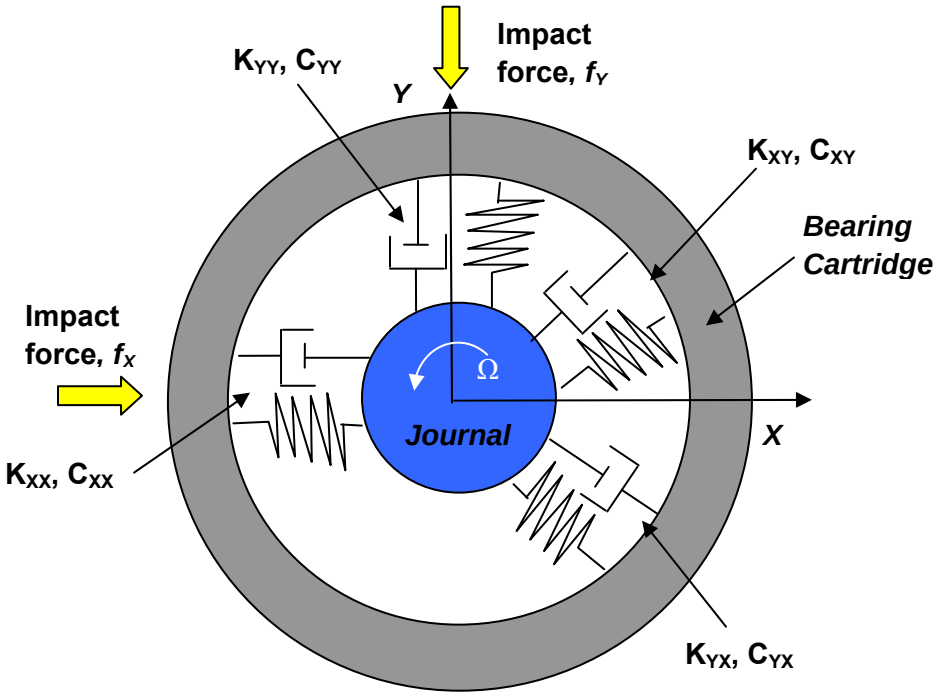

Fig. C.1 Representation of bearing force coefficients and impact forces acting on test bearing

The equations of motion of the test bearing modeled as a 2DOF mechanical system are

$$\begin{pmatrix} f_X - M a_X \\ f_Y - M a_Y \end{pmatrix} = \begin{bmatrix} C_{XX} & C_{XY} \\ C_{YX} & C_{YY} \end{bmatrix} \begin{pmatrix} \delta\dot{x} \\ \delta\dot{y} \end{pmatrix} + \begin{bmatrix} K_{XX} & K_{XY} \\ K_{YX} & K_{YY} \end{bmatrix} \begin{pmatrix} \delta x \\ \delta y \end{pmatrix} \tag{C.1}$$

where $\{f_i\}_{i=X,Y}$ are the excitation forces, M=0.38 kg is the test system mass, $\{a_i\}_{i=X,Y}$ are the accelerations of the bearing cartridge, and $\{K_{ij}, C_{ij}\}_{i,j=X,Y}$ are the bearing stiffness and damping coefficients, respectively. δX and δY are the relative displacements of the bearing with respect to the journal in the horizontal and vertical directions.

Only one of the equations above is needed to identify the stiffness and damping coefficients when the journal does not spin. This is so since cross coupled coefficients are nil without journal

rotation. Thus, the uncoupled equation of motion along one direction (Y) represented in the frequency domain is

$$\frac{F_Y}{Y} = \left[K_{YY} + M * (A_Y / Y)\right] + \left[i\omega C_{YY}\right] \qquad \text{(C.2)}$$

where F_Y, A_Y and Y are the FFTs of the impact force, the bearing accelerations and the relative bearing displacement along the vertical (y) direction. $K_{XX} = K_{YY}$ and $C_{XX} = C_{YY}$ are the identified bearing stiffness and equivalent viscous damping coefficients, and ω is the excitation frequency.

TEST CONFIGURATION

Figure C.2 illustrates the schematic view of the test configuration for identifying the bearing stiffness and damping coefficients along the vertical direction with impact load tests. An eddy current sensor, at one end of the bearing cartridge, measures the bearing displacement with respect to the journal. The model assumes that the whole bearing cartridge remains parallel to the journal. A miniature accelerometer (5.1 g) records the accelerations of the bearing cartridge. Ten impacts are provided in the vertical direction. Frequency domain averages are used to estimate the bearing force coefficients.

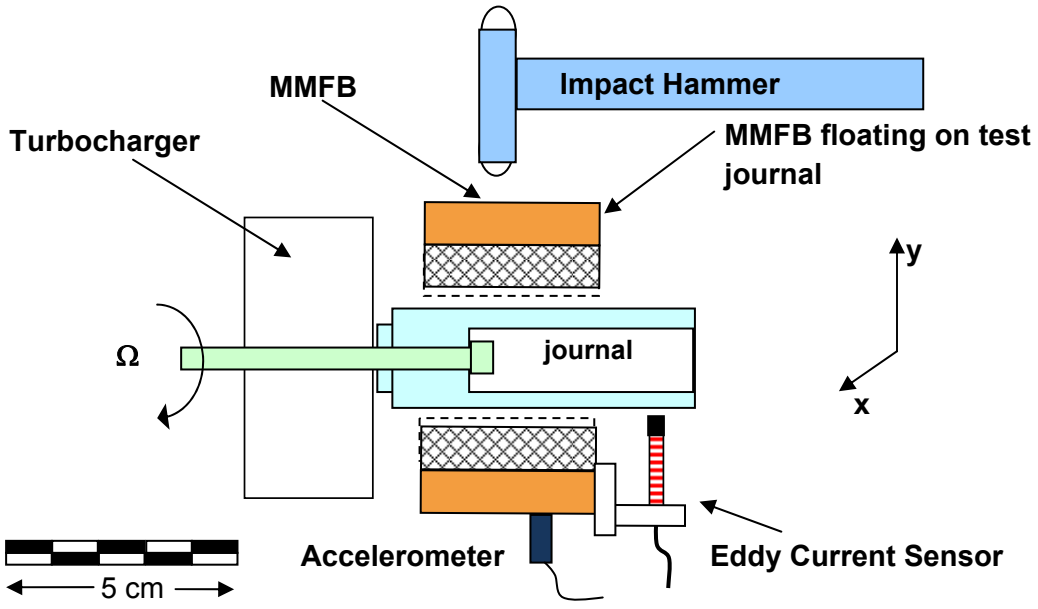

Fig. C.2 Schematic view representing the impact loading of MMFB

IMPACT TEST RESULTS

Figure C.3 shows, for frequencies to 125 Hz, an excellent coherence (~ 1.00) for the displacement due to 10 impact loads. The coherence between the signals is rather poor at higher frequencies as the small impact force does not excite the high frequency bearing displacement components. Figures C.4 and C.5 show the FFTs of the impact force and relative bearing displacement with respect to the shaft, respectively. Note how the displacement amplitudes decrease rapidly as the frequency increases, i.e. the test bearing appears to have large damping.

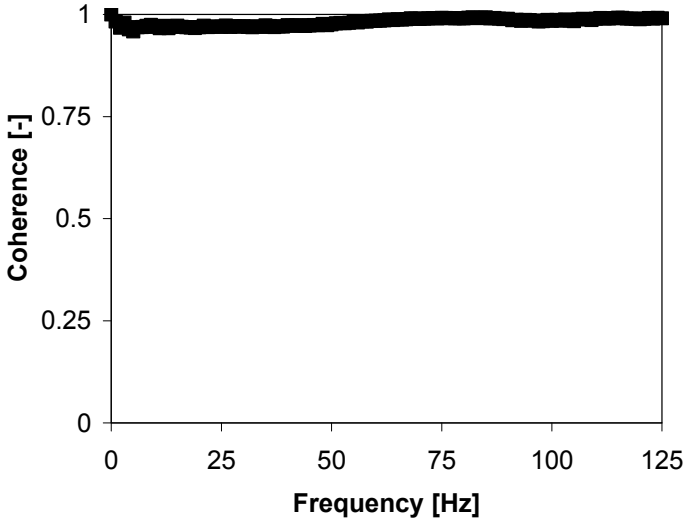

Fig. C.3 Coherence between impact force and eddy current sensor signal. Average of 10 impacts. Journal not rotating

Figure C.6 depicts the FFT of the bearing cartridge acceleration (A_Y) and the derived acceleration, from the relative displacement of the MMFB and the journal, i.e. $|-\omega^2 Y|$. The two accelerations must coincide if the journal is not moving. Alas, this is not the case since the shaft stub of the turbocharger is rather flexible. Hence, the cartridge acceleration must be kept, as measured, in the model for identifying the stiffness and damping coefficients, see Eq. (C2). Substituting $A_Y = -\omega^2 Y$ is not correct.

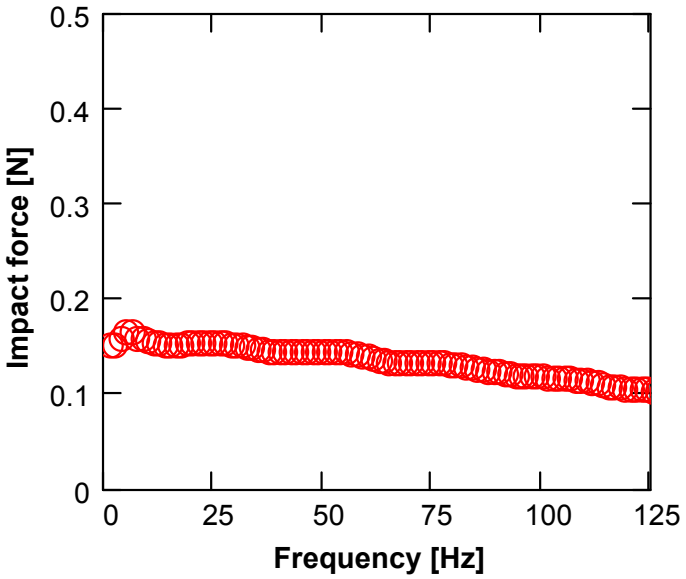

Fig. C.4 FFT of the impact force along the vertical direction. Average of 10 impacts. Journal not rotating.

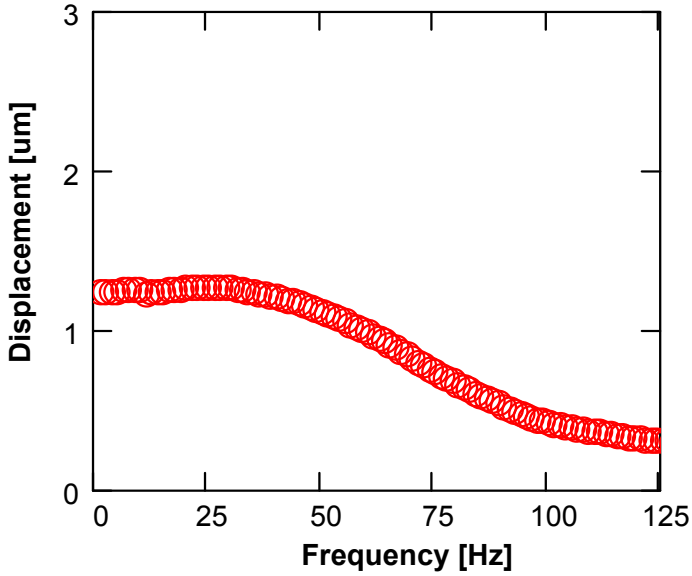

Fig. C.5 FFT of bearing *Y*-displacement with respect to the shaft due to the impact force along the vertical direction. Average of 10 impacts. Journal not rotating.

The bearing model, see Eqn. (C2), includes three unknowns, the bearing stiffness (K_{YY}), the equivalent viscous damping (C_{YY}), and the bearing mass (M). Figure C.7 shows a curve fit of the real part of Eqn. (C2) identifying the bearing *static* stiffness K_{YYo} =0.118 N/μm and system mass M=0.379 kg, which is nearly identical to the measured mass of 0.380 kg, The estimated test

system natural frequency is $f_n = (K_{YY}/M)^{0.5} = 88.8$ Hz, and the system critical damping $C_{crit}=2*(K_{YY}M)^{0.5} = 423$ N.s/m

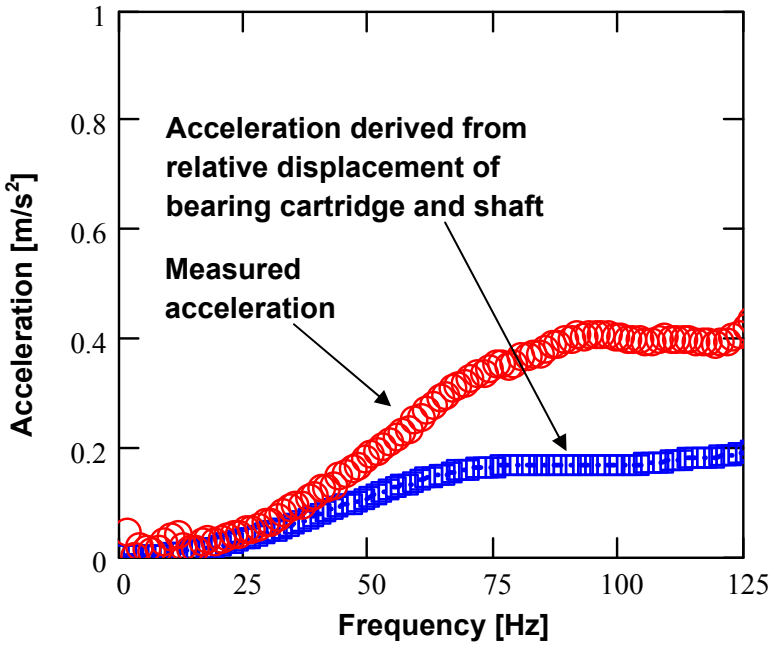

Fig. C.6 FFT of acceleration of bearing cartridge (measured and derived from displacement) versus frequency. Average of 10 impacts. Journal not rotating

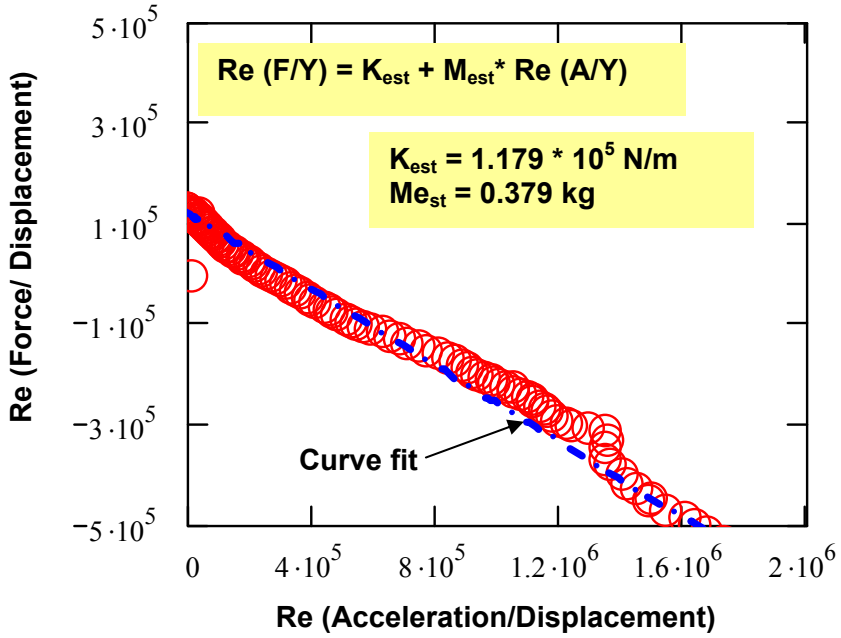

Fig. C.7 (Force/displacement) versus (acceleration/displacement), and curve fit identifying the MMFB stiffness and mass coefficients. Average of 10 impacts. Journal not rotating

Figure C.8 shows the identified bearing stiffness K_{YY} increasing with frequency. Figure C.9 depicts the estimated equivalent viscous damping C_{YY} decreasing from ~ 400 Ns/m to ~200 Ns/m as the frequency increases from 10 to 125 Hz. The damping ratio (C_{YY}/ C_{crit}) decreases from ~ 0.94 to 0.47. In general, the viscous damping in a metal mesh structure is inversely proportional to the frequency and amplitude of motion. See Ref. [6] for further details.

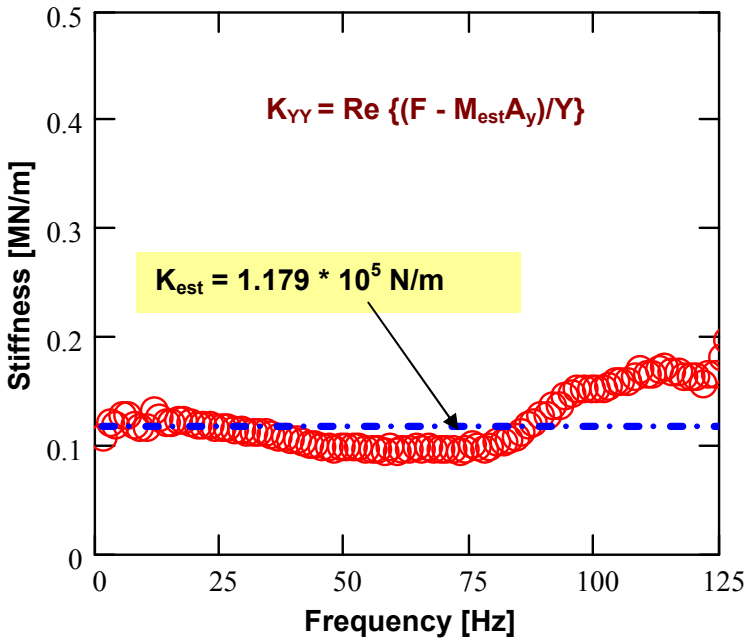

Fig. C.8 Identified MMFB stiffness K_{YY} versus frequency. Journal not rotating

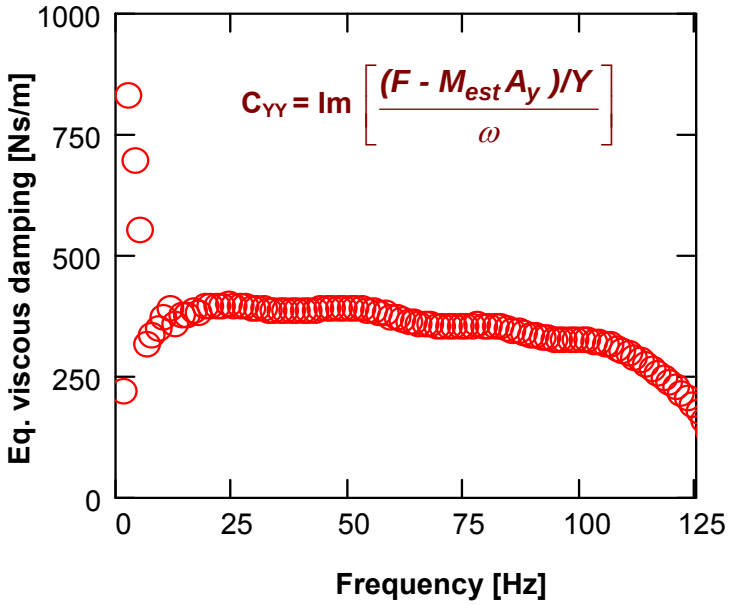

Fig. C.9 Identified MMFB viscous damping C_{YY} versus frequency. Journal not rotating

APPENDIX D. ALUMINUM FOAM BEARINGS

CIATEQ A.C, "Centro de Investigación y Asistencia Tecnologica de el Estado de Queretaro (Mexico)" donated two aluminum foam bearings on 09-25-08. Figure D.1 shows a photograph of the two bearings and Table D.1 lists their dimensions and specifications.

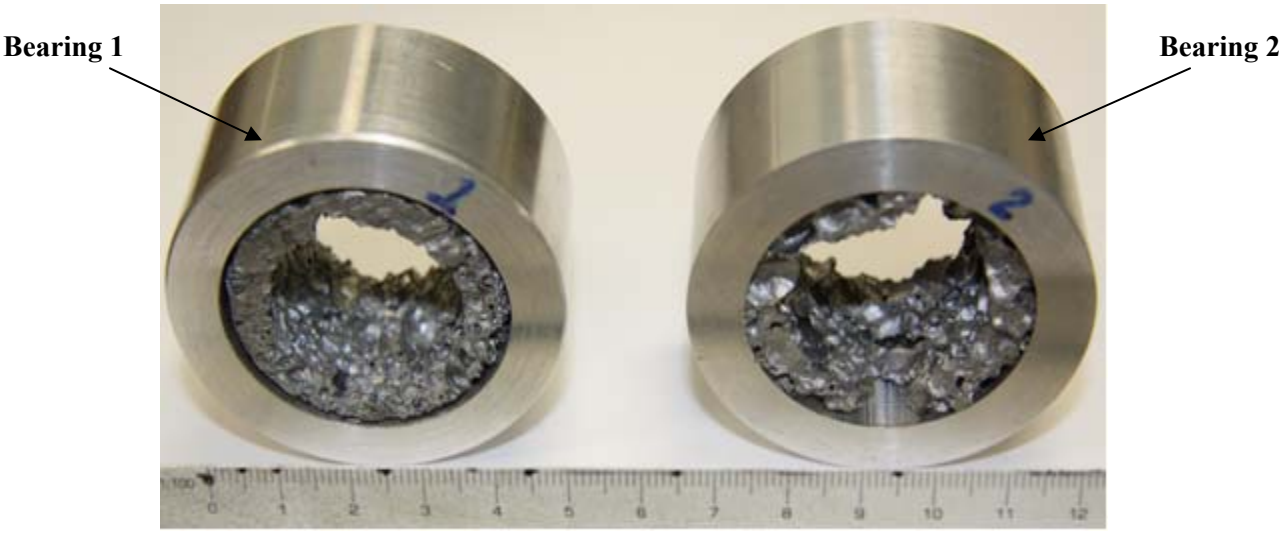

Fig. D.1 Aluminum Foam Bearings

Table D.1 Dimensions and specifications of Aluminum Foam Bearings

Parameters	**Bearing 1**	**Bearing 2**
Bearing Cartridge Outer Diameter, C_o [mm]	58.03 ± 0.01	58.02 ± 0.01
Bearing Cartridge Inner Diameter, C_i [mm]	42.11 ± 0.01	41.60 ± 0.01
Aluminum Foam inner Diameter, F_i [mm]	[28.20, 29.30] [4]	[28.04, 28.15]
Bearing Axial Length, L [mm]	28.07 ± 0.01	28.15 ± 0.01
Bearing Mass, M [kg]	0.1027 ± 0.00005	0.1017 ± 0.00005
Porosity %	86[5]	93
Appearance of Foam	Foam covers almost all the inner surface of the bearing cartridge	Foam covers only ~ 95% of the bearing inner surface

[4] The aluminum foam inner diameter is not a constant along the circumferential direction owing to the rough surface finish. Table 1 shows a range of diameter values.
[5] Porosity computed by considering an Aluminum density of 2.7 g/cc